applied sciences

MDPI

Article

Research on Effective Design Methods of Core Beam of Full Bridge Aeroelastic Model

Kai Qie [1,*], Zhitian Zhang [2], Shouying Li [1] and Yuanyuan Wang [1]

[1] Key Laboratory for Wind and Bridge Engineering of Hunan Province, Hunan University, Changsha 410082, China
[2] College of Civil Engineering and Architecture, Hainan University, Haikou 570100, China
* Correspondence: qiekai@hnu.edu.cn; Tel.: +86-178-0321-1635

Abstract: The trial-and-error method is complex and tedious, but often adapted to determine the cross-section sizes of core beams in the design of reduced-scale models. In this study, two optimization methods, the optimization methods in ANSYS and the genetic algorithm, are investigated to optimize the cross-section sizes of core beams of reduced-scale models, which centers around two targeted moments of inertia and a targeted torsion constant. Due to the difficulty of obtaining an analytical solution of the torsion constant, a series of numerical solutions are proposed. Then, taking a U-shaped cross section as an example, the four geometric sizes of the section are optimized by the ANSYS optimization method and the genetic algorithm, respectively. The results of both methods are in good agreement with the targeted values, but the ANSYS optimization method is prone to fall into the local optimization zone and hence could be easily affected by the initial values. The shortcomings of the ANSYS optimization method can be easily avoided by the genetic algorithm, and it is easier to reach the global optimal solution. Finally, taking a suspension bridge with a main span of 920 m as a prototype, the full-bridge aeroelastic model is designed and the genetic algorithm is used to optimize the cross-section sizes of core beams in the bridge tower and the deck. Natural frequencies identified from the aeroelastic model agree well with the target ones, indicating the structural stiffness, which is provided by the core beams, has been modelled successfully.

Keywords: aero-elastic model; core beam; geometric parameter; genetic algorithm; optimization

Citation: Qie, K.; Zhang, Z.; Li, S.; Wang, Y. Research on Effective Design Methods of Core Beam of Full Bridge Aeroelastic Model. *Appl. Sci.* **2023**, *13*, 5593. https://doi.org/10.3390/app13095593

Academic Editors: Wenli Chen, Donglai Gao and Wen-Han Yang

Received: 7 March 2023
Revised: 20 April 2023
Accepted: 25 April 2023
Published: 30 April 2023

1. Introduction

Suspension bridges and cable-stayed bridges are sensitive to the effect of wind loads, due to their light mass, large flexibility, and small damping [1–5], and the dynamic response of the long-span bridges under wind actions has an increasing relevance as the lengths of the spans grow [6,7]. So, the evaluation of wind resistance performance is essential for large-span bridges and other important structures [8]. Despite computational fluid dynamics [9,10] and semi-analytical approaches [11,12], wind tunnel tests remain the most direct and reliable way that investigates the aeroelastic behavior of a full bridge due to many complex factors [13,14].

Among various reduced-scale models that can be tested in the wind tunnel to study the aeroelastic response of a real bridge, the full-bridge model can more realistically simulate various aerodynamic actions of the real bridge under the action of wind, as well as the interaction between the main vibration modes of the structure [15–17]. A large number of wind tunnel tests on the full-bridge aeroelastic models have been carried out to study the aerodynamic performances of the prototype bridge [18–25]. According to these references, the full-bridge reduced model tests require a faithful representation of the phenomena that are going to be studied when carried out in boundary layer wind tunnels. This requires a series of critical tasks [20,26–28]. One of them is a precise reproduction of the geometry of the model, otherwise slight variations will deeply affect the results [27,29]. Therefore, very high requirements have been put in place throughout the design, and production of the reduced-scale model. The reduced-scale models consist of core beams and "clothing", where the former provides required stiffness, and the latter simulates the aerodynamic configuration [30]. Furthermore, the mass properties of the core beam and the clothing combined should be similar to those of the real bridges. Obviously, the determination of the section geometric parameters of the core beam is particularly important.

Targeted inertial moments of the core beam are calculated based on the similarity relationship with the prototype bridge [30]. The inertial moments of the core beam, including two bending moments of inertia and one torsional constant, are controlled by the section geometric parameters. The inertial moments determined by the section parameters should be as close as possible to the targeted ones.

However, the common cross-sections of the core beams are various, such as rectangular, circular, U-shaped and π-shaped sections [31–33], the ranges of the section geometric parameters are ambiguous. It is difficult to obtain an analytical solution of the torsion constant. Therefore, it is extremely difficult to determine the section geometric parameters of the core beam even if all the targeted inertial moments are modeled accurately. At present, the trial-and-error method is commonly used to determine the section parameters of the core beam, which is complex, is tedious and has low accuracy. The U-shaped cross-section has been the most widely used for core beams of bridge decks, and the rectangular section is generally used for the core beams of bridge towers [33].

In order to determine which geometric parameters of the core beam the model targeted inertial moments effectively, three numerical solutions of the torsion constant are proposed, and two optimization methods for geometric parameters are presented in this study. The first optimization method is the optimization in ANSYS, and the other one is the genetic algorithm. The advantages and disadvantages of the concerned methods are presented.

2. Design of Reduced-Scale Aeroelastic Models

Reduced-scale aeroelastic models are designed and produced (aeroelastic modeling), which aims to reproduce the exact structural dynamic response of the prototype bridge when tested in a wind tunnel. There are four main steps from the actual bridge to the scaled aeroelastic model, as shown in Figure 1. For more details on the design process of reduced-scale aeroelastic models, readers may refer to Ref. [30].

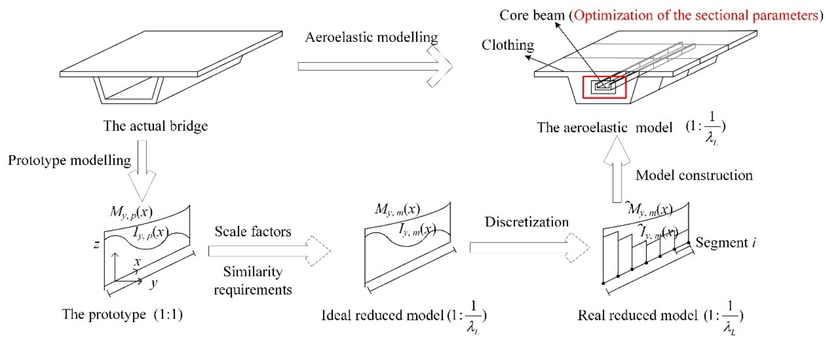

Figure 1. The design process of reduced-scale aeroelastic models.

Step 1. A prototype to the actual bridge is modeled and the dynamic characteristics of the prototype are determined. This prototype has to reproduce the stiffness of the actual bridge in the six degrees of freedom, or at least represent the stiffness in the most representative degree of freedom (the prototype shown as Figure 1).

Step 2. Based on the fundamental relationships between the limiting dimension of the wind tunnel test section and the dimensions of the prototype, the length scale factor λ_L is defined, and the similarity requirements can be determined. Consequently, an ideal reduced-scale model can be defined by employing the scale factors and the similarity requirements.

Step 3. Due to the limitation of model construction, it is difficult to realize the continuous characteristics of the ideal model in the length direction. So, the discretization of continuous properties and simplification of geometric details is necessary. Based on these adjustments, the real reduced model is created and targeted inertial moments are determined, which should be as close as possible to the ideal reduced model.

Step 4. The model production is conducted according to the real reduced model.

In model production, the section parameters of the core beam are determined and the inertial moments calculated by the section parameter should be as close as possible to the targeted ones. A detailed optimization process and numerical solution of the torsion constant are described in detail next.

3. Numerical Solution of Torsion Constant

The cross-section of a core beam commonly used in aeroelastic models is various, rectangular, circular, U-shaped, π-shaped sections and so on. It is difficult to obtain an analytical solution of the torsion constant, so a series of numerical solutions are proposed here. In fact, the finite element method and generalized difference method can deal with the torsion constant for any complex simply connected section, while the five-point difference method is not. For simple simply connected sections, such as rectangular sections, the torsion constant can be obtained by the five-point difference method. For complex simply connected sections, such as U-shaped cross-sections, the torsion constant can be obtained by the generalized difference method or the finite element method.

3.1. Basic Theory

Considering the Prandtl stress function method [34], the two-dimensional elliptic Poisson equation of the first type of Dirichlet boundary value problem for a simply connected section can be obtained as follows:

$$\nabla^2\phi = -2 \tag{1}$$

$$\phi\big|_{\Gamma} = 0 \tag{2}$$

where, ϕ is the stress function, Γ is the boundary of cross-section region Ω. Equation (1) is only applicable in the region Ω, and Equation (2) is valid on the boundary Γ.

The torsion constant D is expressed as a double integral of stress function ϕ in region Ω (including the boundary Γ) as:

$$D = 2\iint_{\Omega}\phi dxdy \tag{3}$$

3.2. Generalized Difference Method

In 1978, Li et al. [35] merged the integral interpolation method into the generalized Galerkin method and thereby extended the irregular grid difference method to the generalized difference. This method not only maintains the simplicity of the difference method, but also has the accuracy of the finite element.

The above method adopts a triangular meshing scheme, as shown in Figure 2. The entire cross-section region Ω is triangularly meshed and the internal angle of each triangle is less than 90°. Taking P_0 in the subregion G_0 as an example, outer nodes around P_0, namely P_1, P_2, P_3, P_4, P_5, and P_6, are selected, and these points are arranged counterclockwise. Meanwhile, six triangles, $P_0P_1P_2$, $P_0P_2P_3$, $P_0P_3P_4$, $P_0P_4P_5$, $P_0P_5P_6$ and $P_0P_6P_1$, are defined by these seven points with point P_0 being their common vertex. The outer centers of these six triangles, q_1, q_2, q_3, q_4, q_5 and q_6, and the adjacent-side midpoints of the six triangles, m_1, m_2, m_3, m_4, m_5 and m_6, define the shaded part G_0, which also is a dual unit.

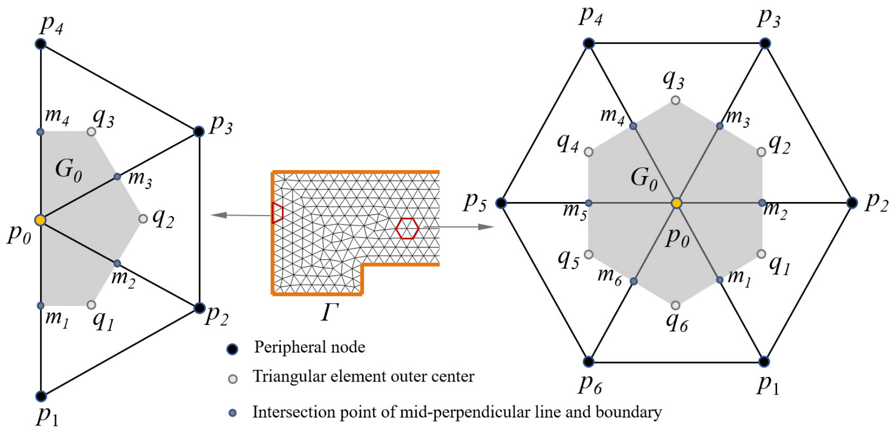

Figure 2. Geometric structure of triangle difference scheme.

For any node inside the region Ω, a difference format is created. Both sides of Equation (1) are integrated over the subdomain G_0:

$$\iint_{G_0} \nabla^2 \phi dxdy = \iint_{G_0} -2dxdy, \tag{4}$$

Using the Green formula, Equation (4) is rewritten as

$$-\int_{\partial G_0} \frac{\partial \phi}{\partial n} ds = \iint_{G_0} -2dxdy \tag{5}$$

where, ∂G_0 is the boundary of the subdomain G_0, and n is the unit normal vector of ∂G_0.

Therefore, the difference format for each point in the subdomain G_0 is obtained as

$$\int_{\partial G_0} \frac{\partial \phi}{\partial n} ds = \sum_{i=1}^{6} \frac{\overline{q_i q_{i+1}}}{\overline{P_0 P_{i+1}}} \cdot \left[\phi(P_{i+1}) - \phi(P_0)\right] + m(G_0) R_{G_0}(\phi), (q_7 = q_1), \tag{6}$$

where, m(G_0) is the area of G_0, $RG_0(\phi)$ is the truncation error.

Substituting Equation (6) into Equation (3) and rounding $RG_0(\phi)$ off, the difference equation of point P_0 is presented as Equation (7):

$$\begin{gathered} -\sum_{i=1}^{6} \frac{\overline{q_i q_{i+1}}}{\overline{P_0 P_{i+1}}} \left[\phi(P_{i+1}) - \phi(P_0)\right] = \iint_{G_0} -2dxdy = m(G_0) \cdot \varphi_0, \\ \varphi_0 = \frac{1}{m(G_0)} \iint_{G_0} -2dxdy \end{gathered} \tag{7}$$

For an arbitrary point on the boundary Γ, the stress function value of P_0, is obtained as

$$\phi(P_0) = 0, \tag{8}$$

The difference equations of all points are formed as a closed system of linear algebraic equations, and its coefficient matrix is symmetric. After solving the equations, the stress results in the region Ω are obtained as shown in Figure 3. According to Equation (3), the double volume of the stress results is the torsion constant of the U-shaped cross-section.

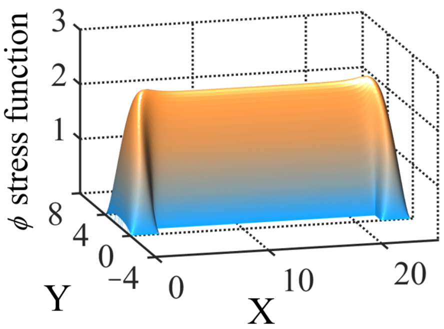

Figure 3. Differential stress function in the region Ω.

3.3. Finite Element Method

The Galerkin method is applied to the variation $\delta\phi$, namely

$$\int_{\Omega}\left(\nabla^2\phi+2\right)\delta\phi dG_0=0, \tag{9}$$

For simply connected sections, the expression is equivalent to the torsion constant when the stress function is 0 at the boundary Γ. So, it is expressed as:

$$J=\int_{\Omega}\frac{1}{2}\cdot\left[\left(\frac{\partial\phi}{\partial x}\right)^2+\left(\frac{\partial\phi}{\partial y}\right)^2\right]dG_0-\int_{\Omega}2\phi dG_0, \tag{10}$$

In the region Ω, the stress function at node i is supposed as ϕi. For any point in the element e, the stress function ϕ can be interpolated as Equation (11), and the partial derivative of the stress function to the coordinate is expressed as Equation (12).

$$\phi=\boldsymbol{N}\boldsymbol{\Phi}_e, \tag{11}$$

$$\begin{Bmatrix}\frac{\partial\phi}{\partial x}\\ \frac{\partial\phi}{\partial y}\end{Bmatrix}=\begin{Bmatrix}\frac{\partial N}{\partial x}\\ \frac{\partial N}{\partial y}\end{Bmatrix}\boldsymbol{\Phi}_e=\boldsymbol{B}\boldsymbol{\Phi}_e{}', \tag{12}$$

where, $\Phi_e=\{\phi_1, \ldots, \phi_n\}^T$ is the stress function vector of the element e, and $N=\{N_1,\ldots, N_n\}$ is the shape function matrix.

Substituting Equations (11) and (12) into (10), and letting $\delta J=0$, leads to the balance equation of the element e, as

$$\boldsymbol{K}_e\boldsymbol{\Phi}_e=\boldsymbol{R}_e, \tag{13}$$

$$\boldsymbol{K}_e=\int_{\Omega}\boldsymbol{B}^T\boldsymbol{B}dG_0, \tag{14}$$

$$\boldsymbol{R}_e=2\int_{\Omega}\boldsymbol{N}^T dG_0 \tag{15}$$

where, $\boldsymbol{K}_e$ and $\boldsymbol{R}_e$ are, respectively, the stiffness matrix and equivalent node loading vector of element e.

Arranging the balance equations of all the elements in region Ω leads to the general balance equation. Typical stress results are shown in Figure 4 by solving the general balance equation. According to Equation (3), the torsion constant is the double volume enclosed by the stress surface and the XY plane.

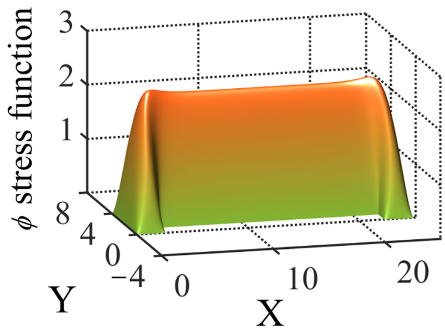

Figure 4. Finite element stress function.

3.4. Five-Point Difference Method

In the five-point difference method, a partial derivative is replaced by the difference quotient of several adjacent numerical points [36], which applies well to a rectangular section. First, a rectangular section is meshed into grids as shown in Figure 5. The edge along the x-axis is divided into N equal segments and the one along the y-axis is divided into M equal segments. Let $x_i = a + ih_1$, $y_j = c + jh_2$, where $0 \le i \le N$, and $0 \le j \le M$. In addition, $\phi_{ij} = \phi(x_i, y_j)$ is defined and the Poisson problem at the inner node is defined as

$$\frac{\partial^2 \phi(x_i, y_j)}{\partial x^2} + \frac{\partial^2 \phi(x_i, y_j)}{\partial y^2} = const(x_i, y_j),\ 1 \le i \le N-1,\ 0 \le j \le M-1, \tag{16}$$

where, const(x_i, y_j) is a constant value equal to −2 in Equation (13).

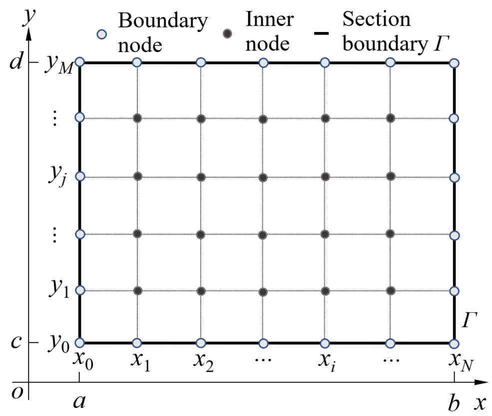

Figure 5. A rectangular cross-section.

The two terms in the left side of Equation (16) are expanded according to the Taylor formula, as

$$\frac{\partial^2 \phi(x_i, y_j)}{\partial x^2} = \frac{1}{h_1^2}\left[\phi(x_{i-1}, y_j) - 2\phi(x_i, y_j) + \phi(x_{i+1}, y_j)\right] - \frac{h_1^2}{12}\frac{\partial^4 \phi(\xi_{ij}, y_j)}{\partial x^4},\ x_{i-1} < \xi_{ij} < x_{i+1} \tag{17}$$

$$\frac{\partial^2 \phi(x_i, y_j)}{\partial y^2} = \frac{1}{h_2^2}\left[\phi(x_i, y_{j-1}) - 2\phi(x_i, y_j) + \phi(x_i, y_{j+1})\right] - \frac{h_2^2}{12}\frac{\partial^4 \phi(x_i, \eta_{ij})}{\partial y^4},\ y_{i-1} < \eta_{ij} < y_{i+1} \tag{18}$$

Substituting Equation (17) and (18) into Equation (16) and ignoring the second order quantity $O(h_1^2 + h_2^2)$, one obtains

$$\frac{1}{h_2^2}\phi_{i,j-1}\frac{1}{h_1^2}\phi_{i-1,j} - 2\left(\frac{1}{h_1^2} + \frac{1}{h_2^2}\right)\phi_{i,j} + \frac{1}{h_1^2}\phi_{i+1,j} + \frac{1}{h_2^2}\phi_{i,j+1} = const(x_i, y_j),\ 1 \le i \le N\text{-}1,\ 0 \le j \le M\text{-}1 \tag{19}$$

The stress function vector ϕ_j is defined as

$$\boldsymbol{\phi}_j = \left(\phi_{1j}, \quad \phi_{2j}, \ldots, \quad \phi_{N-1,j}\right)^{\mathrm{T}}, 0 \le j \le M, \tag{20}$$

and Equation (19) is rewritten as

$$\boldsymbol{D}\boldsymbol{\phi}_{j-1} + \boldsymbol{C}\boldsymbol{\phi}_j + \boldsymbol{D}\boldsymbol{\phi}_{j+1} = \boldsymbol{const}_j, \ 1 \le j \le M-1, \tag{21}$$

$$\boldsymbol{C} = \begin{pmatrix} 2\left(\frac{1}{h_1^2}+\frac{1}{h_2^2}\right) & -\frac{1}{h_1^2} & & & \\ -\frac{1}{h_1^2} & 2\left(\frac{1}{h_1^2}+\frac{1}{h_2^2}\right) & -\frac{1}{h_1^2} & & \\ & \ddots & \ddots & \ddots & \\ & & -\frac{1}{h_1^2} & 2\left(\frac{1}{h_1^2}+\frac{1}{h_2^2}\right) & -\frac{1}{h_1^2} \\ & & & -\frac{1}{h_1^2} & 2\left(\frac{1}{h_1^2}+\frac{1}{h_2^2}\right) \end{pmatrix}, \tag{22}$$

$$\boldsymbol{D} = \begin{pmatrix} -\frac{1}{h_2^2} & & & & \\ & -\frac{1}{h_2^2} & & & \\ & & \ddots & & \\ & & & -\frac{1}{h_2^2} & \\ & & & & -\frac{1}{h_2^2} \end{pmatrix} \tag{23}$$

$$\boldsymbol{const}_j = \begin{pmatrix} const\left(x_1, y_j\right) \\ const\left(x_2, y_j\right) \\ \vdots \\ const\left(x_{N-2}, y_j\right) \\ const\left(x_{N-1}, y_j\right) \end{pmatrix} \tag{24}$$

Note that the first and last terms of vector $const_j$ already contain the boundary conditions at $x = a$ and $x = b$.

Equation (21) can also be expanded to the following matrix form similar to Equation (25), as

$$\begin{pmatrix} \boldsymbol{C} & \boldsymbol{D} & & & \\ \boldsymbol{D} & \boldsymbol{C} & \boldsymbol{D} & & \\ & & \ddots & & \\ & & \boldsymbol{D} & \boldsymbol{C} & \boldsymbol{D} \\ & & & \boldsymbol{D} & \boldsymbol{C} \end{pmatrix} \begin{pmatrix} \boldsymbol{\phi}_1 \\ \boldsymbol{\phi}_2 \\ \vdots \\ \boldsymbol{\phi}_{M-2} \\ \boldsymbol{\phi}_{M-1} \end{pmatrix} = \begin{pmatrix} \boldsymbol{const}_1 - \boldsymbol{D}\boldsymbol{\phi}_0 \\ \boldsymbol{const}_2 \\ \vdots \\ \boldsymbol{const}_{M-2} \\ \boldsymbol{const}_{M-1} - \boldsymbol{D}\boldsymbol{\phi}_M \end{pmatrix} \tag{25}$$

Note that the first and last elements of the vector on the right side of Equation (25) take into account the boundary conditions at $y = c$ and $y = d$.

Difference equations of all points form a closed system of linear algebraic equations, of which the coefficient matrix is symmetric. After solving the equations, stress results can be obtained. A typical solution is shown in Figure 6 and the torsion constant is the double volume enclosed by the stress surface and the XY plane, according to Equation (3).

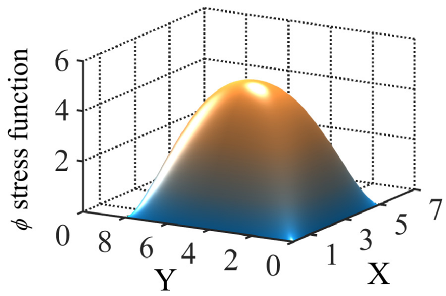

Figure 6. Differential stress function.

4. Geometric Parameters Searching

As shown in Figure 7, a U-shaped cross-section can be divided into three rectangular sections, I, II, and III. Four independent section parameters, *h*, *d*, *th* and *td*, are used to describe section size. According to Figure 6, coordinates of the centroid are obtained as

$$\begin{aligned} \bar{z}_c &= \frac{2d \cdot td(h+th) + 4h \cdot d^2 + td \cdot th}{4h \cdot d + 2td \cdot th} \\ \bar{y}_c &= \frac{2d \cdot h^2 + td \cdot th^2}{4h \cdot d + 2td \cdot th} \end{aligned}, \quad (26)$$

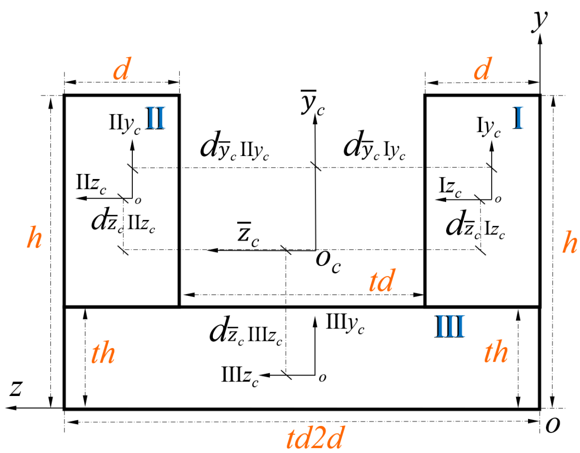

Figure 7. The U cross-section.

The moments of inertia in the *y* and *z* directions, respectively, are given as

$$I_{\bar{y}_c} = \frac{1}{12}\left[2d^3(h-th) + (td+2d)^3 th\right] + d(h-th)\left[(\frac{d}{2}-\bar{z}_c)^2 + (h-\frac{d}{2}-\bar{z}_c)^2\right]^2 + (td+2d)th(\frac{(td+2d)}{2}-\bar{z}_c)^2 \quad (27)$$

$$I_{\bar{z}_c} = \frac{1}{12}\left[2d(h-th)^3 + (td+2d)th^3\right] + 2d(h-th)\left[\frac{1}{2}(h+th)-\bar{y}_c\right]^2 + (td+2d)th(\frac{1}{2}th-\bar{y}_c)^2 \quad (28)$$

The torsion constant of the U-shaped cross section can be determined by the numerical solutions in Section 2.

4.1. Optimization Method by ANSYS

The optimization design module of ANSYS provides two optimization methods, namely the zero-order and the first-order method, which deal with most optimization problems. The zero-order method randomly searches for the optimal solution in a given domain of the dependent variable, while the first-order method uses the first-order partial derivative of the dependent variable. Therefore, the latter is more suitable for local accurate optimization.

Taking a U-shaped cross-section as an example, the target values of three moments of inertia, Target_*Iz*, Target_*Iy* and Target_*Ix*, are listed in Table 1. In fact, the target values listed in Table 1 are based on an actual suspension bridge, which will be mentioned later. In the process of ANSYS optimizing, the initial geometric sizes (*h*, *d*, *th* and *td*) of the section is first assigned, and then *Iz*, *Iy* and *Ix* are calculated.

Table 1. Target section properties.

Target_Iz (mm^4)	*Target_Iy* (mm^4)	*Target_Ix* (mm^4)
79.04	4518.74	241.44

The errors of *Iz*, *Iy* and *Ix* are defined separately as

$$\begin{aligned} Err\_Iz &= 100\% \cdot \left| (\mathrm{Target}\_Iz - Iz) / \mathrm{Target}\_Iz \right| \\ Err\_Iy &= 100\% \cdot \left| (\mathrm{Target}\_Iy - Iy) / \mathrm{Target}\_Iy \right| \\ Err\_Ix &= 100\% \cdot \left| (\mathrm{Target}\_Ix - Ix) / \mathrm{Target}\_Ix \right| \end{aligned} \quad (29)$$

The three errors are all limited to 0~5%. The sum of the three errors is used as an objective function, as

$$TErr = Err\_Iz + Err\_Iy + Err\_Ix, \quad (30)$$

where *Err_Iz* is the sum of the errors of *Iz*, *Iy* and *Ix*.

The purpose of optimization is to minimize the total error. In order to investigate the influence of the initial parameters, two different sets of them and the searching domain are given, as listed in Table 2. It is seen that the initial value of d in the first set is not included in the searching domain. Figure 8 shows the optimization process of the zero-order and the first-order method, where the ordinate is TErr and the abscissa is the number of iterations.

Table 2. Initial values and searching domains.

	h (mm)	*d* (mm)	*th* (mm)	*td* (mm)
Initial set 1	5.038	3.612	3.0579	19.585
Initial set 2	4.138	2.712	3.06	19.6
Searching domain	4.0~7.0	0.1~3.0	1.0~3.99	10.0~30.0
Initial set 1	5.038	3.612	3.0579	19.585

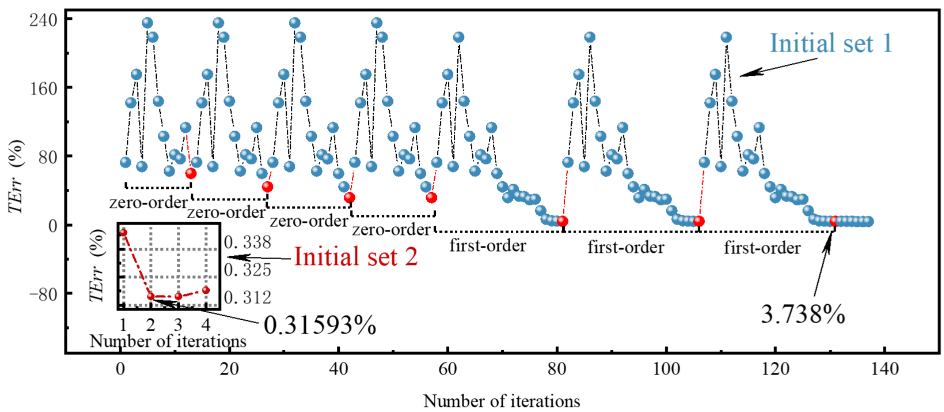

Figure 8. Optimization process.

It can be seen from Figure 8 that, based on the first set of initial values, the parameters are firstly optimized four times by zero-order method, resulting in a total error of 31.318%. Then the first-order method is performed three times, resulting in a total error of 3.738%. However, a total error as small as 0.31593% (see Table 3) is obtained when the second set of initial values is selected and optimized with the first-order method. Comparing the two sets of initial values, it is easy to find that the number of iterations of the second set of initial values is significantly reduced and the accuracy is obviously improved, which indicates that the initial values dominate the total error.

Table 3. ANSYS optimization results of Initial set 2.

Initial Set 2 + First-Order			
h (mm)	*d* (mm)	*th* (mm)	*td* (mm)
4.0378	2.6119	3.0574	19.582
Err_Iz	*Err_Iy*	*Err_Ix*	*TErr*
0.083%	0.003%	0.229%	0.315%

In order to investigate the influence of an individual variable, *h*, *d*, *th* or *td* on the target values in Table 1, the second set of initial values are taken as a reference. The optimization is performed with three variables fixed and the fourth one varies in the given range. The results are plotted in Figures 9–12, where it is noted that *Err_Ix*, *Err_Iy* and *Err_Iz* vary simultaneously. As h increases, *Err_Iz* increases exponentially, while *Err_Iy* and *Err_Ix* are only slightly affected (see Figure 9). The other three cases are similar in the way they change, with the error decreasing first and then increasing to some extent as Figures 10–12 show. Hence, each variable has an optimal value that minimizes the three errors at the same time. The optimal values of *h*, *d*, *td*, and *th* in their own dimensionless searching domain are 0, 0.9, 0.44, 0.67, respectively. Figure 13 shows the effects of the four variables on the total error *TErr*. It can be seen that *TErr* is relatively large except for four cases, which agrees well with the results in Figures 9–12.

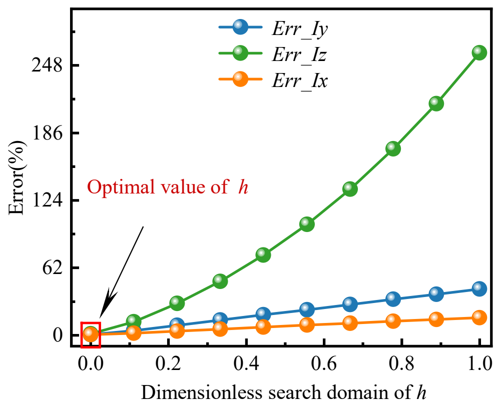

Figure 9. The errors caused by h.

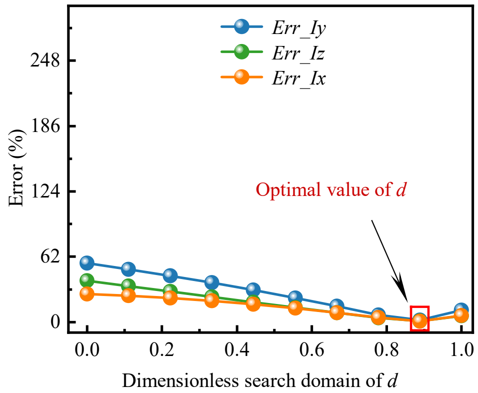

Figure 10. The errors caused by d.

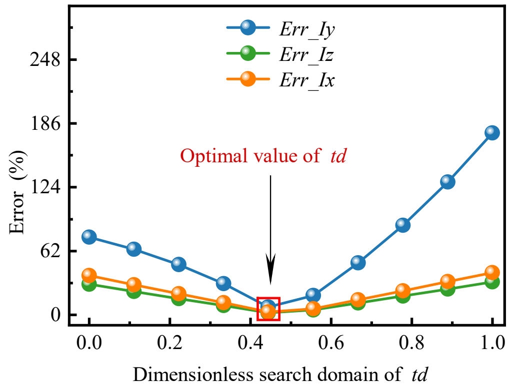

Figure 11. The errors caused by td.

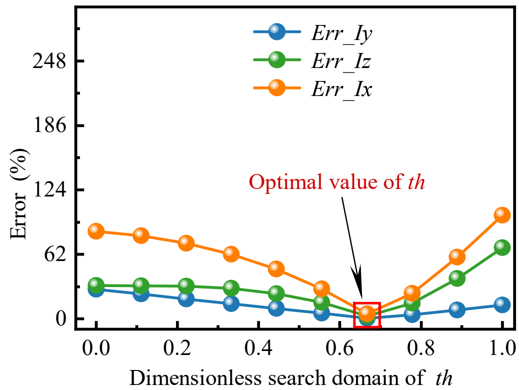

Figure 12. The errors caused by th.

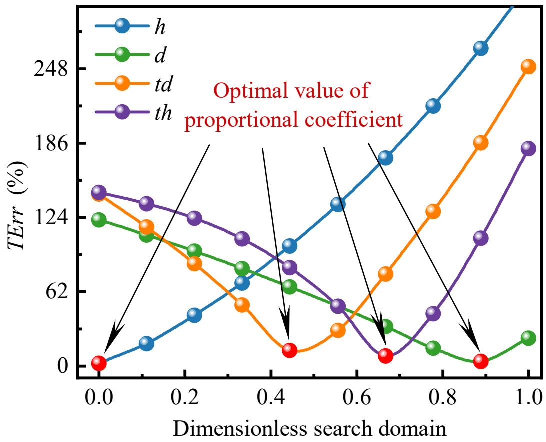

Figure 13. Total errors.

4.2. Genetic Algorithm

Due to the sensitivity of the zero-order and the first-order method to initial values, it is favorable to introduce a genetic algorithm to the optimization process. A genetic algorithm is a method based on the theory of biological evolution and developed by Holland [37]. One of its advantages is that it does not require the calculation of a function gradient in the process of optimization. In addition, it can be easily extended to a global optimization [38]. For more details on the terminology and algorithm, readers may refer to Refs. [39,40].

By using the global search ability of the genetic algorithm, the concerned problem can be converted into minimizing the total error expressed as

$$TErr = Err\_Iz + Err\_Iy + Err\_Ix, \tag{31}$$

where *TErr* is the total error. Ranges of the four variables must be restricted as: $a \le t \le b$, $c \le d \le d$, $e \le th \le f$, $g \le td \le h$.

The genetic algorithm still takes the target values in Table 1 as optimization objectives. Additionally, it is noted that the initial values are not needed in this case. Figure 14 shows the genetic algorithm optimization process, and it shows that the average fitness value gradually approaches the maximum fitness value, which indicates that the possible solution approaches the optimal solution. Meanwhile, the best fitness value, which is the total error, converges to 0.47% at the 70th iteration. In addition, the mean distance between individuals, representing the diversity of offspring, decreases with the increase of the number of iterations of optimization, and approaches 0 at the 40th iteration. Table 4 shows the optimization results, which shows high accuracy of the genetic algorithm.

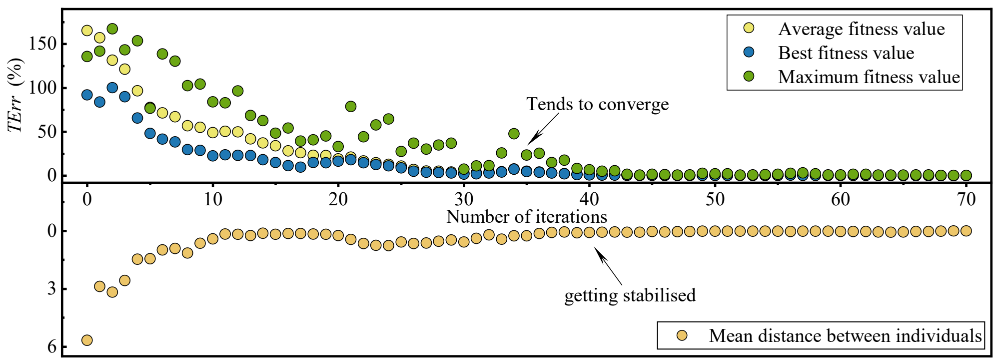

Figure 14. Genetic algorithm optimization process.

Table 4. Optimization results of genetic algorithm.

Moment of Inertia	Target Values (mm^4)	Optimized (mm^4)	Error (%)	Final geometric sizes (mm)		
					h	4
I_z	79.05	79.34	0.37		d	2.62
I_y	4518.74	4518.70	0.09		th	3.09
I_x	241.44	241.42	0.01		td	19.57

It is concluded that the zero-order and the first-order method leads to uncertainties results, which is affected by the initial values. The performance of the genetic algorithm is steady, converges rapidly and has high precision.

5. Practical Application

Taking a suspension bridge with a main span of 920 m as a prototype, the whole optimization process of the core beams in the full bridge reduced-scale model is represented. The overall layout of the suspension bridge is shown in Figure 15, and the cross-section of the steel box girder is shown in Figure 16.

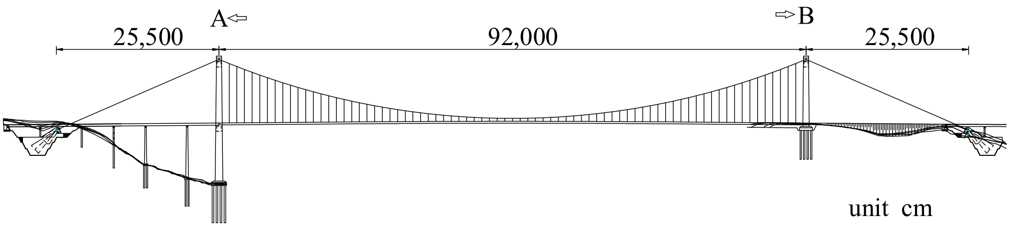

Figure 15. Layout of bridge span.

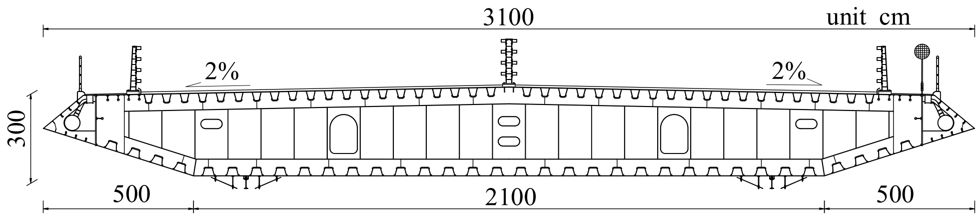

Figure 16. Main girder section.

Considering the limiting dimensions of the wind tunnel (length × width × height: 15 × 8.5 × 2 m), the geometric scale of the scaled model to the prototype is 1:121. In addition to the geometric similarity, the aeroelastic model and the real bridge should meet the similarity of mass distribution, stiffness and damping characteristics that determine the similarity of dynamic characteristics. Based on these similarity requirements, the similarity ratio of the bending and torsion stiffness with the prototype is $1:121^5$, shown in Table 5. The main cable is designed based on the principles of similar stiffness, mass, and quasi-steady wind load. The hangers are tensile components, and the diameters of the hangers are determined by the principle of similar tensile stiffness. The full-bridge reduced-scale model is shown in Figure 17. The aeroelastic model adopts a combination of core beams enwrapped in "clothing", which simulate aerodynamic configurations. The core beams provide the required rigidity, and the clothing simulates the aerodynamic configurations.

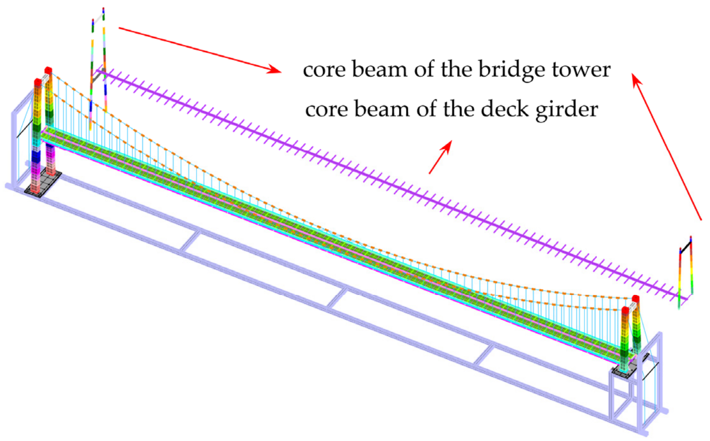

Figure 17. The full bridge reduced-scale model.

Table 5. Similarity ratios based on similarity relationship.

Parameter	Unit	Similarity Ratio
Length	m	1:121
Wind Speed	m/s	1:11
Frequency	Hz	11: 1
Time	s	1:11
Mass per unit length	Kg/m	$1:121^2$
Moment of inertia per unit mass	Kg·m^2/m	$1:121^4$
Bending stiffness	N·m^2	$1:121^5$
Torsional stiffness	N·m^2	$1:121^5$
Axial stiffness	N	$1:121^3$

5.1. Core Beam Design of the Deck Girder

In this section, the U-shaped section is used for the core beam of the deck girder. Based on the similarity ratio of $1:121^5$ for the bending and torsion stiffness, the targeted inertia moments and torsion constant of the core beam can be obtained listed in Table 6. The genetic algorithm is used to optimize the section parameters of the core beam, and the optimization results of the section parameters are also listed in Table 6. The results show the parameters of the U-shaped section are defined as 4, 2.62, 3.09, and 19.57 mm, and the total error is as low as 0.47%. The overall size of the U-shaped section of the core beam is given in Figure 18.

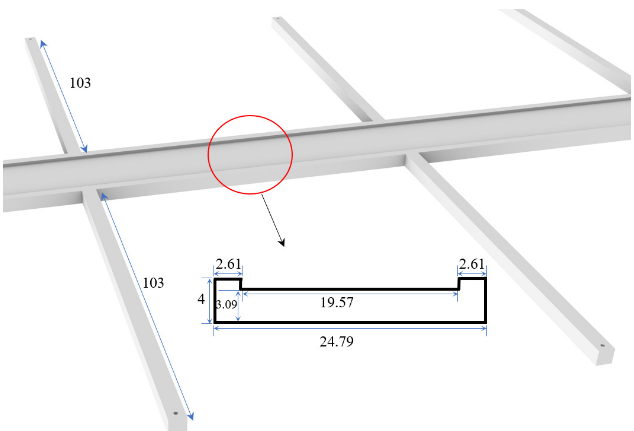

Figure 18. Overall sizes of the core beam of the deck girder (mm).

Table 6. Section characteristics of main beam and steel core beam.

Moment of Inertia	Prototype (m^4)	model (mm^4)		error (%)			
		Required	Realized			h	4.00
I_z	2.05	79.05	79.34	0.37	Section sizes (mm)	d	2.61
I_y	117.20	4518.74	4518.70	0.09		th	3.09
I_x	6.26	241.44	241.42	0.01		td	19.57

It is not feasible to directly test the torsional frequency of the entire core beam. Therefore, a 1498.6 mm-long core beam was subjected to finite element analysis and experimental test in order to verify the accuracy of the torsional stiffness, as shown in Figure 19. One end of the core beam is fixed, and the attenuation time history in three directions were obtained to analyze the modal frequencies as shown in Figures 20–22. The targeted frequencies from finite element analysis and the tested frequencies are listed in Table 7. It can be found that there is little error between the targeted and the tested frequencies, which verifies that the design of the core beam is feasible.

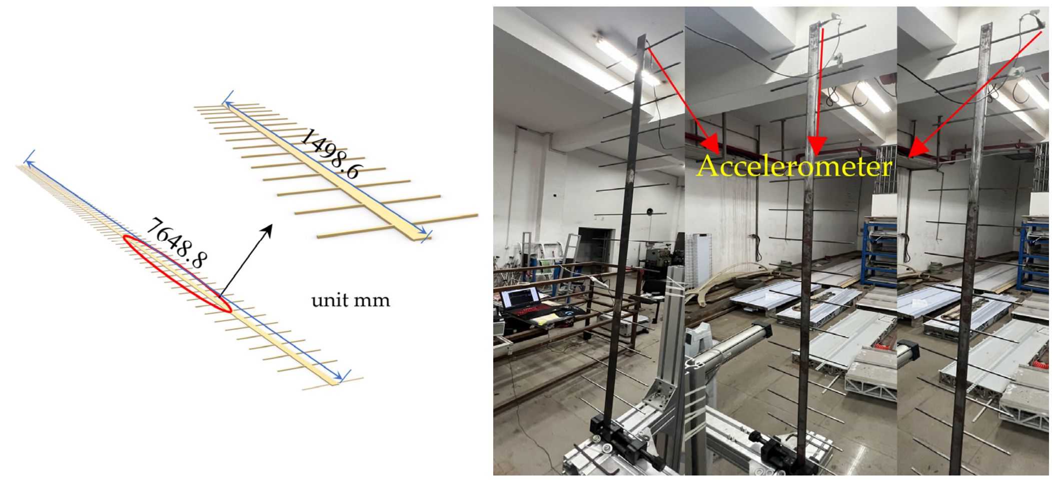

(**a**) the core beam section (**b**) the test photo

Figure 19. The model test of the core beam section.

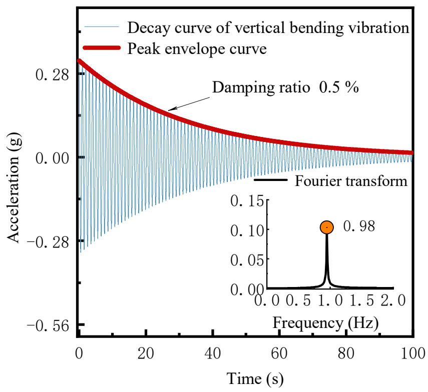

Figure 20. Time history of vertical-bending-free decay.

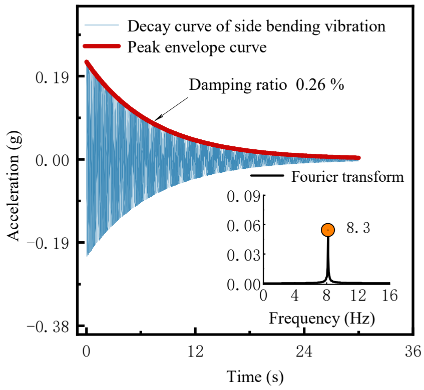

Figure 21. Time history of side-bending-free decay.

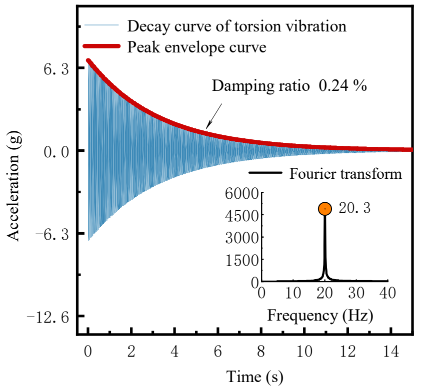

Figure 22. Time history of torsion-free decay.

Table 7. Major modal properties of the tower models.

	Mode	Targeted (Hz)	Measured (Hz)	Error (%)
core beam of the deck girder	1st-Vertical bending	1.00	0.98	−1.93
	1st-Side bending	8.47	8.3	−2.04
	1st-Torsional	20.49	20.3	−0.93

5.2. Core Beam Design of the Bridge Tower

The rectangular section is used for the cross-section of the bridge tower, the sizes of which vary vertically along the tower height. Due to the changing nature of the tower, it is discretized into ten segments, as shown in Figure 23. The section dimensions of each segment are averaged over its length. In so doing, tower B has ten groups of section properties as the targeted values. The optimization is accomplished by the genetic algorithm, of which the results are listed in Table 8. According to the properties listed in Table 8, the core beams of the bridge towers are manufactured as shown in Figure 24. The tested torsional and vertical acceleration time histories of the core beam of tower B are given in Figures 25 and 26, and the natural frequencies can be obtained by Fourier transforms.

When mass properties are concerned, it can be seen from Table 9 that additional mass is needed for all segments to meet the similarity of mass distribution with the prototype. This is realized by winding thin lead sheets around the core beams. Finally, the aeroelastic models of the two towers are shown in Figure 27. The tested torsional and vertical acceleration time histories of tower B are given in Figures 28 and 29, and the corresponding spectral analysis is also presented. All the tested frequencies and the theoretical ones of the models of bridge tower A and bridge tower B are listed in Table 10 and it shows that the tested frequencies agree very well with the targeted values.

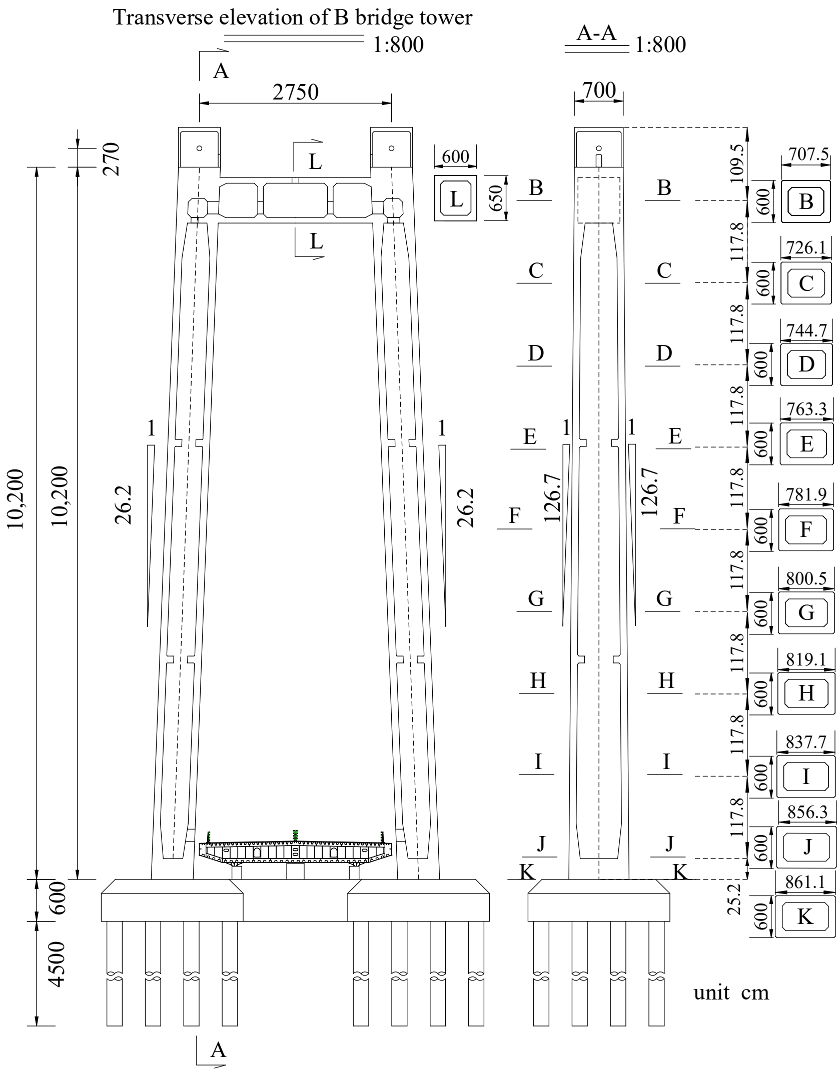

Figure 23. The elevation and sectional views of bridge tower B.

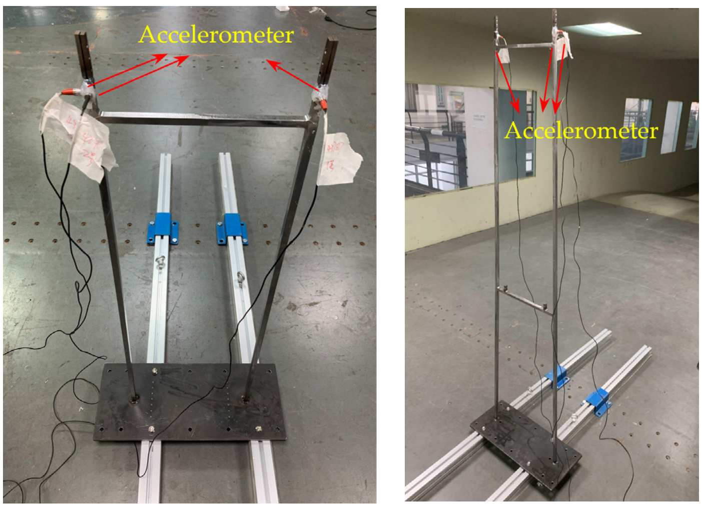

(**a**) (**b**)

Figure 24. The core beam model test of bridge tower A and B. (**a**) The core beam of bridge tower B. (**b**) The core beam of bridge tower A.

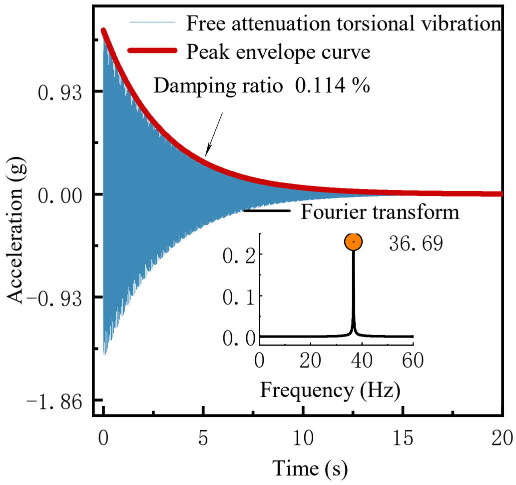

Figure 25. Time history of torsion-free decay of tower B.

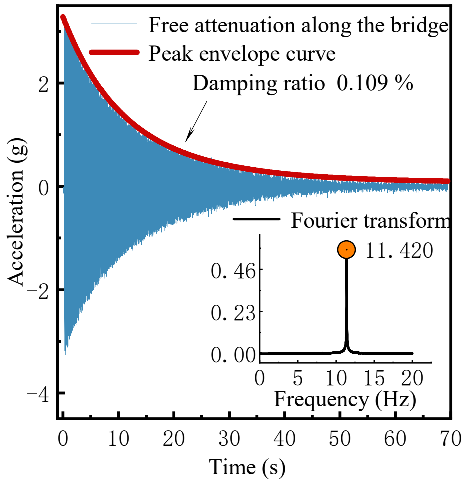

Figure 26. Time history of bending-free decay.

Table 8. Geometric sizes of core beam sections of bridge tower B.

Segment	Moment of Inertia				Core Beam Section (mm)		Error (%)	
	Prototype (m^4)		Model (mm^4)					
	Iz	*Ix*	*Iz*	*Ix*	Width	Height	*Iz*	*Ix*
B-top	135.35	203.95	571.72	954.86	9.15	8.95	0.14	0.03
B-C	144.89	212.61	848.96	1426.5	10.09	9.93	0.20	0.35
C-D	154.83	221.31	907.98	1486.0	10.34	9.86	0.03	0.30
D-E	165.18	230.05	969.42	1545.7	10.56	9.89	0.05	0.32
E-F	175.93	238.83	1033.3	1605.7	10.80	9.84	0.01	0.08
F-G	187.10	247.65	1099.7	1666.0	11.02	9.84	0.37	0.08
G-H	198.69	256.49	1168.7	1726.4	11.27	9.81	0.01	0.01
H-I	210.71	265.36	1240.2	1787.1	11.49	9.80	0.03	0.14
I-J	223.17	274.27	1314.4	1848.0	11.77	9.73	0.51	0.51
J-K	226.43	276.55	1362.0	1886.3	11.88	9.75	0.03	0.33
L	84.29	145.63	510. 7	997.42	8.55	9.80	0.04	0.35

Table 9. Mass per unit length of bridge tower B.

Segment	Prototype (kg)	Required for the Model (g)	Core Beam (g)	Total Mass of Thin Lead Sheets and Clothing (g)

B-top	278,150.32	157.01	58.14	98.87
B-C	670,724.55	378.61	76.58	302.03
C-D	681,692.03	384.80	77.94	306.85
D-E	692,659.52	390.99	79.77	311.21
E-F	703,627.00	397.18	81.23	315.95
F-G	714,594.48	403.37	82.81	320.56
G-H	725,561.97	409.56	84.46	325.11
H-I	736,529.45	415.75	86.11	329.64
I-J	747,496.93	421.94	87.50	334.45
J-K	192,097.71	108.43	22.54	85.89
L	1,249,633.13	705.39	151.53	553.85

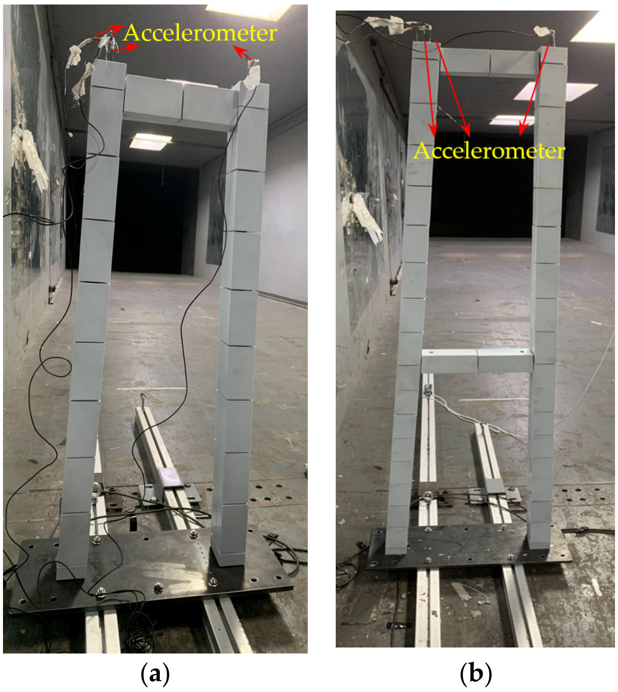

Figure 27. Model test of the bridge towers. (**a**) The model of bridge tower B. (**b**) The model of bridge tower A.

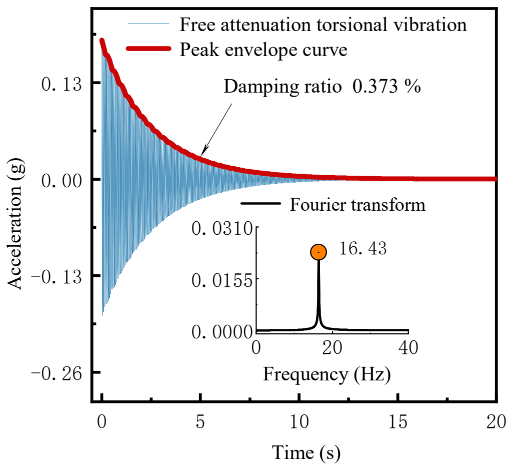

Figure 28. Tested time history of torsion-free decay.

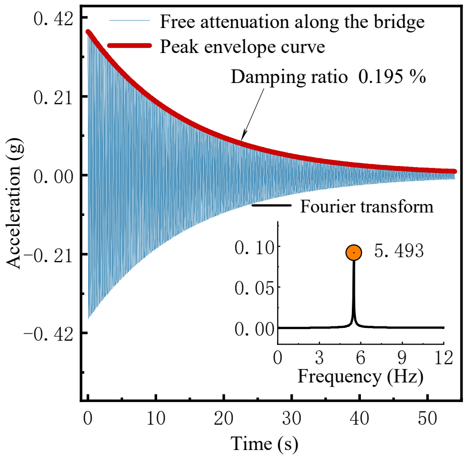

Figure 29. Acceleration Time history of bending-free decay.

Table 10. Major modal properties of the tower models.

	Mode	Targeted (Hz)	Measured (Hz)	Error (%)
A-core beam	1st-Vertical bending	4.226	4.321	2.25
A-core beam	1st-Torsional	19.82	20.117	1.48
B-core beam	1st-Vertical bending	11.551	11.42	1.13
B-core beam	1st-Torsional	36.66	36.69	0.08
A-bridge tower	1st-Vertical bending	1.913	1.953	2.11
A-bridge tower	1st-Torsional	8.678	8.789	1.28
B-bridge tower	1st-Vertical bending	5.405	5.493	1.63
B-bridge tower	1st-Torsional	16.529	16.43	0.60

5.3. The Dynamic Characteristics Testing of the Aeroelastic Model

The dynamic characteristics test of the aeroelastic model is shown in Figure 30. Laser displacement meters and accelerometers are arranged at the quarter span length and half span length, which can collect different modal vibration information. Low-order modes are excited at different excitation positions, and vibration signals are collected to determine the frequencies. The test results are listed in Table 11. It is worth mentioning that due to the first-order antisymmetric torsional frequency reaching 6.302 Hz, manual excitation cannot excite the vibration, while the bridge state flutter is controlled by a positive symmetric vibration mode, which can meet the test requirements.

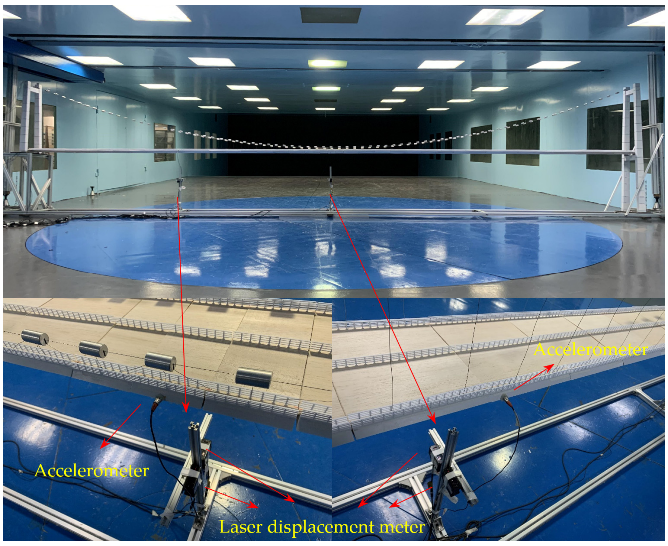

Figure 30. Aeroelastic model dynamic characteristics testing.

Table 11. Major frequency characteristics of the full-bridge aeroelastic model.

Mode	Targeted (Hz)	Measured (Hz)	Error (%)
1st-Positive symmetrical vertical bending	1.859	1.818	−2.234
1st-Antisymmetric vertical bending	1.280	1.270	−0.795
1st-Positive symmetrical torsional	4.582	4.430	−3.323
1st-Positive symmetrical lateral bending	6.302	/	/
1st-Positive symmetrical lateral bending	0.874	0.879	0.4801
1st-Antisymmetric lateral bending	2.804	2.734	−2.483

6. Conclusions

In this study, numerical solutions of torsion constant of simply-connected sections are presented, two effective core beam design methods are proposed to address the difficulties in the design of reduced-scale models, and the proposed methods are verified with an aeroelastic model of an actual suspension bridge. The conclusions are summarized as follows:

(1) For simple simply connected sections, such as rectangular sections, the simple five-point difference method is recommended to determine the torsion constant. For complex simply connected sections, such as U-shaped cross sections, the generalized difference method and finite element method can be used to determine the torsion constant.

(2) For the ANSYS optimization method, the initial values of the section parameters of the core beams are required. If the initial values are not well-designed, the ANSYS optimization method is prone to fall into a local optimal solution. This study derives the numerical solution method for the torsion constant of rectangular and U-shaped sections commonly used in aeroelastic models, and proposes the genetic algorithm in the form of the total error of the section parameters. Through the optimization process, it is found that the genetic algorithm is easy to find out with the global optimization solution. It not only converges at a fast speed, but also leads to results of high quality and reliability. Since the investigated concerns can deal with any reduced-scale model, the proposed solution is of general validity and can be extended to many other different cases.

Each part in the design of an aeroelastic model is crucial to perfectly examine the aerodynamic performance of the full bridge in a wind tunnel, and these parts play different roles but are closely related. This study only provides meaningful research on the optimization design of the cross-sectional size of the core beam. However, different scaled models or simplified aerodynamic shapes may have significant differences in their aerodynamic performance, which means there is still a long way to go for future research on the rationality of scaled and simplified aerodynamic shapes.

Author Contributions: K.Q. and Z.Z. conceived the idea of this research; K.Q., wrote the paper; S.L. and Y.W. reviewed and revised the paper. All authors have read and agreed to the published version of the manuscript.

Funding: This research was funded by the National Natural Science Foundation of China (Grant Number 51578233 and 51938013).

Data Availability Statement: The data, models, and codes that support the findings of this study are available from the corresponding author.

Conflicts of Interest: The authors declare no conflicts of interest.

References

1. Khamprapai, W.; Tsai, C.-F.; Wang, P. Analyzing the Performance of the Multiple-Searching Genetic Algorithm to Generate Test Cases. *Appl. Sci.* **2020**, *10*, 7264. https://doi.org/10.3390/app10207264.
2. Astiz, M.A. Flutter Stability of Very Long Suspension Bridges. *J. Bridge Eng.* **1998**, *3*, 132–139. https://doi.org/10.1061/(asce)1084-0702(1998)3:3(132).
3. Ito, M. Cable-stayed Bridges: Recent Developments and Their Future. In Proceedings of the Seminar, Yokohama, Japan, 10–11 December 1991.
4. Nagai, M.; Fujino, Y.; Yamaguchi, H.; Iwasaki, E. Feasibility of a 1,400 m Span Steel Cable-Stayed Bridge. *J. Bridge Eng.* **2004**, *9*, 444–452. https://doi.org/10.1061/(asce)1084-0702(2004)9:5(444).
5. Xu, Y.-L. *Wind Effects on Cable-Supported Bridges*; John Wiley & Sons: Hoboken, NJ, USA, 2013. https://doi.org/10.1002/9781118188293.
6. Scanlan, R. The action of flexible bridges under wind, I: Flutter theory. *J. Sound Vib.* **1978**, *60*, 187–199. https://doi.org/10.1016/s0022-460x(78)80028-5.
7. Scanlan, R. The action of flexible bridges under wind, II: Buffeting theory. *J. Sound Vib.* **1978**, *60*, 201–211. https://doi.org/10.1016/s0022-460x(78)80029-7.
8. Bernuzzi, C.; Crespi, P.; Montuori, R.; Nastri, E.; Simoncelli, M.; Stochino, F.; Zucca, M. Resonance of steel wind turbines: Problems and solutions. *Structures* **2021**, *32*, 65–75. https://doi.org/10.1016/j.istruc.2021.02.053.
9. Cochran, L.; Derickson, R. A physical modeler's view of computational wind engineering. *J. Wind Eng. Ind. Aerodyn.* **2011**, *99*, 139–153.
10. Nieto, F.; Owen, J.S.; Hargreaves, D.M.; Hernández, S. Bridge deck flutter deriv-atives: Efficient numerical evaluation exploiting their interdependence. *J. Wind Eng. Ind. Aerodyn.* **2015**, *136*, 138–150.
11. Wu, T.; Kareem, A. Bridge aerodynamics and aeroelasticity: A comparison of modeling schemes. *J. Fluids Struct.* **2013**, *43*, 347–370. https://doi.org/10.1016/j.jfluidstructs.2013.09.015.
12. Kareem, A.; Wu, T. Wind-induced effects on bluff bodies in turbulent flows: Nonstationary, non-Gaussian and nonlinear features. *J. Wind Eng. Ind. Aerodyn.* **2013**, *122*, 21–37. https://doi.org/10.1016/j.jweia.2013.06.002.
13. Diana, G.; Resta, F.; Zasso, A.; Belloli, M.; Rocchi, D. Forced motion and free motion aeroelastic tests on a new concept dynamometric section model of the Messina suspension bridge. *J. Wind Eng. Ind. Aerodyn.* **2004**, *92*, 441–462. https://doi.org/10.1016/j.jweia.2004.01.005.
14. Diana, G.; Rocchi, D.; Argentini, T. An experimental validation of a band superposition model of the aerodynamic forces acting on multi-box deck sections. *J. Wind Eng. Ind. Aerodyn.* **2013**, *113*, 40–58. https://doi.org/10.1016/j.jweia.2012.12.005.
15. LaRose, G.; Davenport, A.; King, J. Wind effects on long span bridges: Consistency of wind tunnel results. *J. Wind Eng. Ind. Aerodyn.* **1992**, *42*, 1191–1202. https://doi.org/10.1016/0167-6105(92)90126-u.
16. Diana, G.; Falco, M.; Bruni, S.; Cigada, A.; Larose, G.; Darnsgaard, A.; Collina, A. Comparisons between wind tunnel tests on a full aeroelastic model of the proposed bridge over Stretto di Messina and numerical results. *J. Wind Eng. Ind. Aerodyn.* **1995**, *54–55*, 101–113. https://doi.org/10.1016/0167-6105(94)00034-b.
17. Zasso, A.; Cigada, A.; Negri, S. Flutter derivatives identification through full bridge aeroelastic model transfer function analysis. *J. Wind Eng. Ind. Aerodyn.* **1996**, *60*, 17–33. https://doi.org/10.1016/0167-6105(96)00021-9.
18. Hui, M.C.; Larsen, A.; Falbe-Hansen, K. Full aeroelastic model tests for Stonecutters bridge. *IABSE Symposium Report*; International Association for Bridge and Structural Engineering: Zurich, Switzerland, 2004; pp. 72–77.
19. Saeed, A.T.; Liang, Z.L.; Yun, Y.Z.; Zoubi, F.A.; Salih, O.A. Full Model Wind Tunnel Study on the Xia-Zhang Bridge Under Operation Stage. *Am. J. Eng. Appl. Sci.* **2010**, *3*, 390–395. https://doi.org/10.3844/ajeassp.2010.390.395.
20. Fujino, Y.; Ito, M.; Shino, I.; Iwamoto, M.; Hikami, Y.-I.; Tatsumi, M.; Miyata, T. Wind tunnel study of long-span suspension bridge under smooth and turbulent flow. *J. Wind Eng. Ind. Aerodyn.* **1990**, *33*, 313–322. https://doi.org/10.1016/0167-6105(90)90046-f.
21. Xiang, H.; Chen, A.; Song, J. On wind resistant properties of Tiger Gate suspension bridge. *Wind Struct.* **1998**, *1*, 67–75. https://doi.org/10.12989/was.1998.1.1.067.
22. Gu, M.; Chen, W.; Zhu, L.; Song, J.; Xiang, H. Flutter and buffeting responses of the Shantou Bay Bridge. *Wind Struct.* **2001**, *4*, 505–518. https://doi.org/10.12989/was.2001.4.6.505.
23. Irwin, P.A.; Stoyanoff, S.; Xie, J.; Hunter, M. Tacoma Narrows 50 years later—Wind engineering investigations for parallel bridges. *Bridge Struct.* **2005**, *1*, 3–17. https://doi.org/10.1080/1573248042000274551.
24. Zhu, L.; Wang, M.; Wang, D.; Guo, Z.; Cao, F. Flutter and buffeting performances of Third Nanjing Bridge over Yangtze River under yaw wind via aeroelastic model test. *J. Wind Eng. Ind. Aerodyn.* **2007**, *95*, 1579–1606. https://doi.org/10.1016/j.jweia.2007.02.019.
25. Argentini, T.; Diana, G.; Rocchi, D.; Somaschini, C. A case-study of double multi-modal bridge flutter: Experimental result and numerical analysis. *J. Wind Eng. Ind. Aerodyn.* **2016**, *151*, 25–36. https://doi.org/10.1016/j.jweia.2016.01.004.
26. Davenport, A.; King, J. The influence of topography on the dynamic wind loading of long span bridges. *J. Wind Eng. Ind. Aerodyn.* **1990**, *36*, 1373–1382. https://doi.org/10.1016/0167-6105(90)90133-w.
27. Irwin, P.A. Bluff body aerodynamics in wind engineering. *J. Wind Eng. Ind. Aerodyn.* **2008**, *96*, 701–712. https://doi.org/10.1016/j.jweia.2007.06.008.

28. Schewe, G.; Allan L. Reynolds Number Effects in the Flow around a Bluff Bridge Deck Cross Section. J. Wind Eng. Ind. Aerodyn. 1998, 74-76, 829–38. https://doi.org/10.1016/s0167-6105(98)00075-0.
29. Mannini, C.; Šoda, A.; Voß, R.; Schewe, G. Unsteady RANS simulations of flow around a bridge section. *J. Wind Eng. Ind. Aerodyn.* **2010**, *98*, 742–753. https://doi.org/10.1016/j.jweia.2010.06.010.
30. Montoya, M.C.; King, J.; Kong, L.; Nieto, F.; Hernández, S. A method for improving the dynamic response of full bridge reduced-scale models in aeroelastic wind tunnel tests by using optimization algorithms. *J. Wind Eng. Ind. Aerodyn.* **2017**, *167*, 198–216. https://doi.org/10.1016/j.jweia.2017.04.003.
31. Ge, Y.; Xia, J.; Zhao, L.; Zhao, S. Full Aeroelastic Model Testing for Examining Wind-Induced Vibration of a 5,000 m Spanned Suspension Bridge. *Front. Built Environ.* **2018**, *4*, 20. https://doi.org/10.3389/fbuil.2018.00020.
32. Diana, G.; Rocchi, D.; Argentini, T. Buffeting response of long span bridges: Numerical-experimental validation of fluid-structure interaction models. In Proceedings of the IABSE Conference: Structural Engineering: Providing Solutions to Global Challenges, Geneva, Switzerland, 23–25 September 2015.
33. Li, G.H.; Wang, W.J.; Ma, X.C.; Zuo, L.B.; Wang, F.B.; Li, T.Z. Wind Tunnel Test Study on Pipeline Suspension Bridge via Aeroelastic Model with π Connection. *J. Pipeline Syst. Eng. Pract.* **2019**, *10*, 04018025. https://doi.org/10.1061/(asce)ps.1949-1204.0000333.
34. Conti, E.; Grillaud, G.; Jacob, J.; Cohen, N. Wind effects on the Normandie cable-stayed bridge: Comparison between full aeroelastic model tests and quasi-steady analytical approach. *J. Wind Eng. Ind. Aerodyn.* **1996**, *65*, 189–201. https://doi.org/10.1016/s0167-6105(95)00040-2.
35. Timoshenko, S.P.; Goodierwrited, J.N. *Theory of Elasticity*, 3rd ed.; McGraw-Hill Book Company: New York, NY, USA, 1970.
36. Li, R. A survey on the generalized defference method and its application. *Acta Sci. Nat. Univ. Jilinensis* **1995, 01: 14–22**. (In Chinese)
37. Zhang, X. *Matlab Efficient Solution of Differential Equations: Principle and Realization of Spectral Method*; China Machine Press: Beijing, China, 2016. (In Chinese)
38. Holland, J.H. *Adaptation in Natural and Articial Systems*; University of Michigan Press: Ann Arbor, MI, USA, 1975.
39. Yang, Z.N.; Wu, Z. W. .; Lei, T.A. A comparision between ANSYS optimization and GA in the truss structure. *Tech. Autom. Appl.* **2004**, *07*, 4–6+12. (In Chinese)
40. Deb, K.; Sundar, J. Reference Point Based Multi-Objective Optimization Using Evolutionary Algorithms. In Proceedings of the 8th Annual Conference on Genetic and Evolutionary Computation, GECCO '06, Seattle, WA, USA, 8–12 July 2006; ACM: New York, NY, USA, 2006.